IEEE Access
Multidisciplinary ⋮ Rapid Review ⋮ Open Access Journal

Received 27 January 2023, accepted 14 February 2023, date of publication 22 February 2023, date of current version 27 February 2023.

Digital Object Identifier 10.1109/ACCESS.2023.3247011

RESEARCH ARTICLE

Deep Learning Based Design Methodology for Electric Machines: Data Acquisition, Training and Optimization

BIKRANT POUDEL, (Graduate Student Member, IEEE), AND EBRAHIM AMIRI, (Senior Member, IEEE)
Department of Electrical and Computer Engineering, The University of New Orleans, New Orleans, LA 70148, USA
Corresponding author: Ebrahim Amiri (eamiri@uno.edu)

This work was supported by the Louisiana Board of Regents under Award AWD-10000076.

ABSTRACT This paper presents an automated deep learning-based design methodology to facilitate the design and optimization processes in electro-mechanical energy conversion devices. To validate the generality of the model, a complex machine structure with hybrid Permanent Magnets (PMs) is selected as the case study. First, the machine's geometrical topology and the respective design variables are described in the cylindrical coordinate system and programmed into a Finite Element (FE) software package. Next, the program sweeps through the predefined ranges of selected design variables and captures corresponding air-gap flux distribution through an automated FE-based parametric analysis. The air-gap flux density data is post-processed and fed into a deep neural network (DNN) training algorithm. In particular, 10,000 data sets are utilized for training the DNN model. The trained model successfully predicts the machine's performance for any random set of parameters, as confirmed via FE. Finally, by leveraging the trained model, the structural parameters of the machine are optimized to limit higher-order spatial flux harmonics and the cogging torque.

INDEX TERMS Data acquisition, deep learning, finite element, permanent magnet machine.

I. INTRODUCTION

Replacing a portion of high-energy Permanent Magnets (PMs) with low-energy PMs, generally known as hybrid PM (rare-earth (RE) + ferrite) machines, is an effective solution to lower the manufacturing cost in PM machines [1]. However, the partial removal of high-energy PMs without proper design adjustments could lower the overall torque capacity. In addition, the hybrid structure requires a coordinated distribution between the two types of PMs to ensure a smooth operation [1]. Such sophisticated design considerations could impose a high computational burden and may not be easily achievable with classical design methods. Although, with the advancement in computing technology and Finite element (FE) based simulation software platforms in recent years, the processing time for design, analysis and optimization of electromagnetic devices has been rapidly declining, the classical FE-based parametric design process relies on trial and error to search for and locate the proper design. Such manual efforts could be time-consuming, may not deliver the most optimal design, and may not even be practical in complex cases with a high number of design variables such as PM machines with hybrid magnetic structures.

Although the optimal design solution could to some extent get automated through deploying systematic optimization algorithms [2], [3], [4], it requires a computationally heavy repetitive time-domain process to determine the optimal set of parameters. This is because the main electromagnetic characteristics of the machine such as flux distribution, back-emf, and the torque profile are captured through extensive time-stepping transient analysis. Although FE models can be paired up with analytical modeling to avoid excessive computations [5], analytical models are typically established based on a set of simplifying assumptions. In addition, analytical models are limited in the sense that they could be applied only to certain type(s) of electric machines. For example, state of

The associate editor coordinating the review of this manuscript and approving it for publication was Valentine Novosad.

the art two-dimensional subdomain model is not suitable for structures that lack cylindrical symmetry such as interior PM machines [6].

Alternatively, Deep Neural Network (DNN)-based models can be adopted for the analysis and optimization of electrical machinery systems without requiring extensive time-domain analysis. In [7], a DNN model is trained to predict the response of a conventional PM machines. However, the implemented solution uses the cross-sectional image of the motor to feed the machine topology into the training algorithm. This would require a significant number of input data (pixel points) to construct colored images. DNN models are also developed and utilized for purposes other than design and optimization such as predicting the efficiency map of electric machine drives [8] or fault detection applications [9].

In this paper a hybrid PM machine with novel magnetic structure is proposed. To facilitate design, analysis and optimization, a DNN model is established and applied to the proposed machine. First, geometrical design parameters (within the predefined design ranges) are fed into the FE model to generate a sufficient number of training data sets (10,000) for the DNN model. The training data sets are generated in the form of primitive magnetic flux density through an automated parametric analysis in FE magnetostatic solver. Next, the trained model is utilized to predict the primitive magnetic flux density for a given set of design parameters. The magnetic flux density waveform is multiplied with the complex permeance function to obtain the modulated air-gap flux density. Lastly, the trained model is utilized to optimize structural parameters with objective functions set as ''limited higher order spatial flux harmonic'' and ''low cogging torque''. The accuracy of the trained model is confirmed through a series of comparative FE analysis. The paper is organized as follows. Section II describes the structure of the proposed machine and the respective geometrical formulation. Section III presents the FE implementation procedure, data acquisition, and the DNN algorithm. Section IV presents results, discussion and optimization followed up by concluding remarks in Section V.

II. MACHINE DESCRIPTION AND GEOMETRICAL FORMULATION

Fig. 1 schematically illustrates the structure of standard hybrid Surface Mounted PM (SPM) machine, and the respective Magneto-Motive Force (MMF) waveform [4]. Due to the different magnetic energy/strength of the RE (in red) and ferrite (in blue) magnets the MMF waveform is given in the form of a step function. This implies that the primitive airgap flux density of the standard hybrid PM machine contains rich higher order spatial harmonics [5], which leads to higher harmonic torque [10], [11]. In addition, cogging torque in PM machines is generated as a result of the interaction between PM flux and variable permeance (due to stator slotting) in the air gap, and is computed by the rate of change of magnetic energy in the airgap as expressed in (1) [12]. Higher order flux harmonics interact with the variable permeance of the airgap

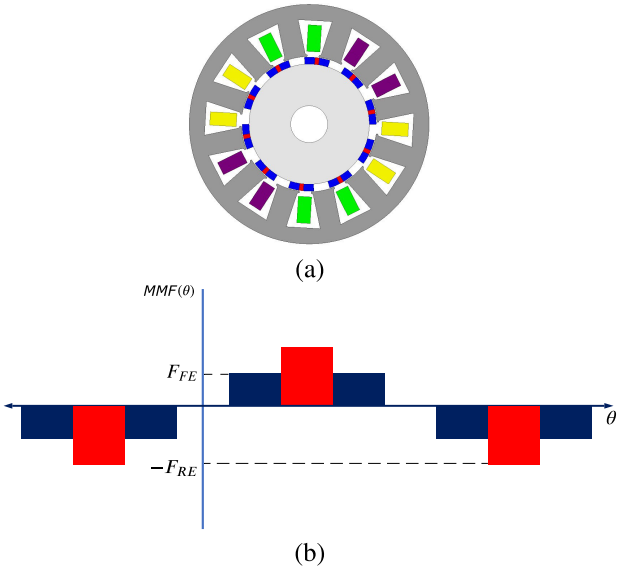

FIGURE 1. Schematic of the hybrid SPM machine with RE and ferrite magnets (a) rotor and stator topology [4], (b) MMF waveform of the hybrid SPM machine.

at a different rate/frequency and may ultimately contribute to a higher cogging torque.

$$T(\alpha) = -\frac{\delta W(\alpha)}{\delta(\alpha)} \tag{1}$$

$$W(\alpha) = \frac{1}{2\mu}\int_V B^2\, dV \tag{2}$$

where, W is the magnetic energy of the machine, α is the rotor position, B is the rotor flux density modulated by the stator permeance, and μ is the permeability.

Motivated by these performance considerations and to form a near-sinusoidal PM flux distribution in the airgap a novel structure of hybrid SPM machine is proposed and used as the case study.

Fig. 2 shows the schematic of the proposed machine where rare-earth PMs are highlighted with red and ferrite PMs with a blue color. Design data for the proposed machine is presented in Table 1. Ferrite PMs are arranged to form an inset magnet structure for a better flux concentration, and better protection against demagnetization and centrifugal forces at high speed runs [13]. In addition, the surface mounted rare-earth PMs are partially enclosed by the ferrite PMs to boost the mechanical strength of the rotor structure. Since the structure includes two types of PMs with different energy levels, it requires a coordinated magnetic arrangement between the two PM types to form a near sinusoidal magnetic flux density in the airgap. This is essential to avoid undesirable effects such as higher harmonic distortion level, higher cogging torque, and potentially higher torque ripple.

It is essential to consider all geometrical parameters and generate sufficient number of data to establish a well-trained predictive DNN model. For this purpose and to facili-

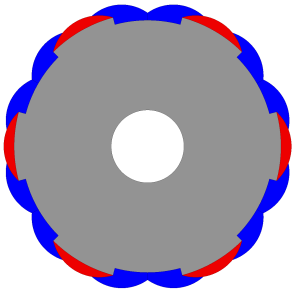

FIGURE 2. Rotor layout of the proposed structure.

TABLE 1. Machine design data.

Slot number	36
Pole number	6
Stator outer diameter	145 mm
Air-gap length	0.5cm
Stack length	65 mm
RE-PM material	NdFe35
Non RE-PM material	Ferrite
Magnet reminance of RE-PM	1.01 T
Magnet reminance of Ferrite-PM	0.332 T

tate/automate the FE parametric analysis, geometrical design parameters are formulated and programmed into the FE solver. This includes the size/dimension and the geometry of the two types of PMs and the rotor core. The solver sweeps through the specified ranges of design parameters to generate/collect required number of data for the training stage. Design parameters are visually illustrated in Fig. 3, where

- R_r is the radius of rotor
- h_f is the height of ferrite PM, the trapezoidal section *ABCD*
- θ_1 is the angular length of the trapezoidal section *ABCD*
- θ_2 is half the angular length of inner arc of rare-earth PM *DHI*
- F is the center of semi-circle *DJI* (the outer arc of rare-earth PM)
- E is the center of semi-circle *AG*
- α and δ control the radius of semi-circles *AG* and *DJI*
- θ_{arc} is half the angular length of outer arc of rare-earth PM *DJI*.

A. GEOMETRICAL FORMULATION OF FERRITE PM ABCD

The key geometrical data points (i.e., A, B, C and D) of ferrite PM, section *ABCD* (shown in Fig. 3) are formulated in cylindrical coordinate system and presented in (3)-(6).

$$A = (R_r cos(\theta_1 + \theta_2), R_r sin(\theta_1 + \theta_2)) \tag{3}$$

$$B = ((R_r - h_f)cos(\theta_1 + \theta_2), (R_r - h_f)sin(\theta_1 + \theta_2)) \tag{4}$$

$$C = ((R_r - h_f)cos(\theta_2), (R_r - h_f)sin(\theta_2)) \tag{5}$$

$$D = (R_r cos(\theta_2), R_r sin(\theta_2)) \tag{6}$$

B. GEOMETRICAL FORMULATION OF FERRITE PM AGD

The key geometrical data points required to formulate ferrite PM, section *AGD* include data points A (3), E (7) and the radii R_{AE} (8) as shown in Fig. 3. This is because section *AGD* is

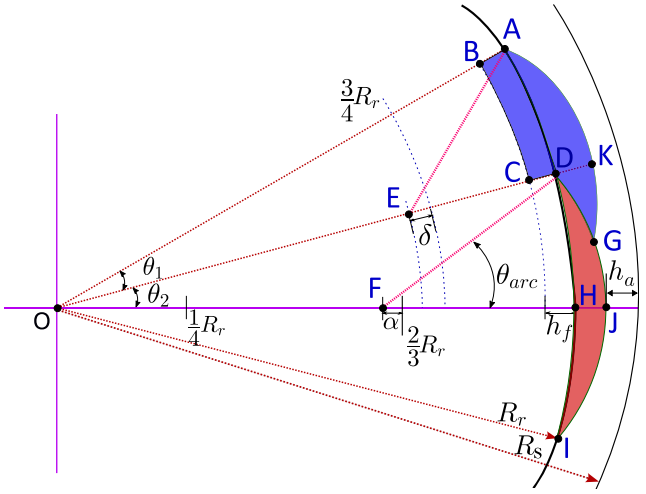

FIGURE 3. Geometry of motor design.

located along the perimeter of a hypothetical circle centered at point E and radii R_{AE}. The circle is then subtracted from the union of rotor and the outer arc of the rare-earth PM *DJI* to form the section *AGD*.

$$E = ((\frac{3}{4}R_r - \delta)cos(\theta_1)(\frac{3}{4}R_r - \delta)sin(\theta_1)) \tag{7}$$

$$R_{AE} = \sqrt{\begin{array}{l}(R_r cos(\theta_1 + \theta_2) - (0.75R_r - \delta)cos(\theta_2))^2 \\ +(R_r sin(\theta_2 + \theta_2) - (0.75R_r - \delta)sin(\theta_2))^2\end{array}} \tag{8}$$

The maximum distance between ferrite and rare-earth PMs (sections *AGD* and *DJI*) from the center of the rotor (i.e., reference point O) is also a key design parameter since it helps to determine the inner radius of the stator and the length of the air-gap. The maximum distance between PM section *AGD* and the rotor center (marked as point K in Fig. 4) occurs at the intersection of line OK and the green colored circle centered at point E (Fig. 4). The location of point K in Cartesian X-Y plane is given by (9):

$$K_x = E_x + \frac{E_x \times R_{AE}}{\sqrt{E_x^2 + E_y^2}}$$

$$K_y = E_y + \frac{E_y \times R_{AE}}{\sqrt{E_x^2 + E_y^2}} \tag{9}$$

where E_x and E_y are the coordinates of point E in X-Y plane. The distance of point K from the rotor center ($O = (0, 0)$) is marked as R_{OK} and takes the following form (10):

$$R_{OK} = \sqrt{K_x^2 + K_y^2} \tag{10}$$

C. GEOMETRICAL FORMULATION OF OUTER ARC OF RARE-EARTH PM DJI

The key geometrical data points required to formulate outer arc of rare-earth PM *DJI* include data points D (6), F (11) and the arc angle θ_{arc} (12) as shown in Fig. 3. This is because section *DJI* is located along the perimeter of a hypothetical

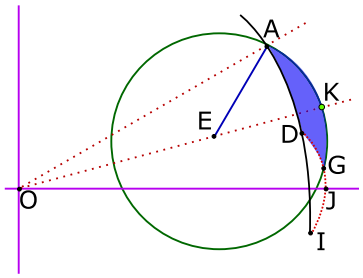

FIGURE 4. The geometric coordinate of point *K* (the intersection of semi circle *AJ* and line *OK*).

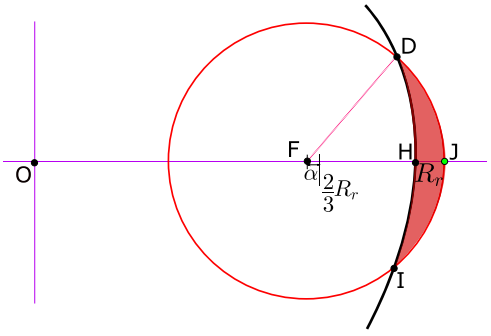

FIGURE 5. The geometric coordinate of point *J* (the intersection of semi circle *DJI* and line *OJ*).

semi-circle centered at point F and $(-2\times\theta_{arc})$ arc angle from starting/reference point D. The inner arc of rare-earth PM, section (DHI) is located along the perimeter of a hypothetical semi-circle centered at point $O = (0, 0)$ and $(-2 \times \theta_2)$ arc angle from starting/reference point D. The inner and outer arcs are then united to form the rare-earth PM.

$$F = \left((\tfrac{2}{3}R_r - \alpha), 0\right) \tag{11}$$

$$\theta_{arc} = tan^{-1}\left(\frac{R_r sin(\theta_2)}{R_r cos(\theta_2) - (\frac{2}{3}R_r - \alpha)}\right) \tag{12}$$

The maximum distance between rare-earth PM and the rotor center (marked as point J in Fig. 5) occurs at the intersection of line OJ and the red colored circle centered at point F (Fig. 5). The location of point J in Cartesian X-Y plane is given by (13):

$$\begin{aligned} J_x &= \left(\frac{2}{3}R_r - \alpha\right) + R_{FD} \\ J_y &= 0 \end{aligned} \tag{13}$$

where R_{FD} is radius of the red circle. The distance of point J from the rotor center $(O = (0, 0))$ is marked as R_{OJ} and takes the following form (14).

$$R_{OJ} = J_x \tag{14}$$

The higher length between R_{OK} (10) and R_{OJ} (14) is selected to determine the inner radius of stator.

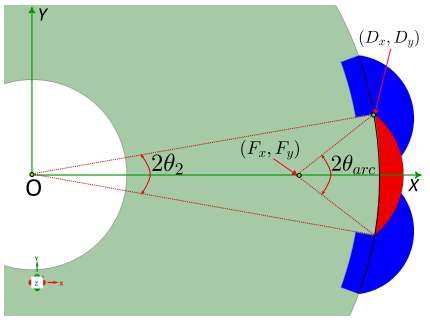

FIGURE 6. FE software implementation of RE magnet.

III. FE SOFTWARE IMPLEMENTATION AND DATA ACQUISITION

This section explains the procedural steps for implementation of the structural and geometrical design data into the FE software and data acquisition for the DNN training.

A. IMPLEMENTATION OF THE FORMULATED STRUCTURAL AND GEOMETRICAL DESIGN DATA INTO THE FE SOFTWARE

Fig. 6 illustrates one rotor pole of the hybrid PM machine implemented in the FE Software. The corresponding design data for the entire machine is presented in Table 2. The FE implemented design data sets for inner and outer arc of the rare-earth PM (i.e., starting point, center of the arc and angular length of the arc) are presented in Table 3 and Table 4, respectively. The ''negative'' angle in Table 3 and 4 indicates clockwise angular sweep of the arc starting from the initial point (point A for ferrite PM and point D for rare-earth PM) along the center (point E for ferrite PM and point F for rare earth PM).

Similarly based on the design steps included in Section II, the blue colored ferrite PM is implemented in the FE software. The maximum limit of angles θ_1 and θ_2 are chosen based on the number of poles and can be expressed as $\theta_{max} = \pi/N_r$, where N_r is the number of rotor poles. Similarly, the values of α and δ are chosen such that the PM doesn't completely lie inside the rotor and have a valid geometry.

B. DATA ACQUISITION AND DEEP LEARNING

The goal is to create a well-trained model that can accurately relate geometrical parameters to the electromagnetic performance of the machine and predict the machine response for any random set of parameters. The target output considered in the training is the magnetic flux distribution in the air-gap. The reason for choosing air-gap flux density as the target is because the key electromagnetic performance of the machine such as back electromotive force, electromagnetic torque, and cogging torque can be achieved by having the knowledge of air-gap magnetic flux distribution. To establish a properly trained model sufficient number of data points must be generated and fed to the model. This is accomplished by running (e.g., 10000) parametric analysis in FE software considering

TABLE 2. Structural design data set implemented in the FE model.

Name	Value	Unit
R_r	55	mm
θ_1	15	deg
θ_2	15	deg
A_{1x}	$R_r * cos(\theta_1)$	
A_{1y}	$R_r * sin(\theta_1)$	
h_f	5	mm
B_{1x}	$(R_r - h_f) * cos(\theta_1)$	
B_{1y}	$(R_r - h_f) * sin(\theta_1)$	
C_{1x}	$R_r - h_f$	
C_{1y}	0	mm
D_{1x}	R_r	
D_{1y}	0	mm
D_x	$R_r * cos(\theta_2)$	
D_y	$R_r * sin(\theta_2)$	
α	-10	mm
θ_{arc}	$abs(atan((R_r * sin(\theta_2))/((2 * R_r/3 - \alpha) - (R_r * cos(\theta_2)))))$	
F_x	$2 * R_r/3 - \alpha$	
F_y	0	mm
A_x	$R_r * cos(\theta_1 + \theta_2)$	
A_y	$Rr * sin(\theta_1 + \theta_2)$	
δ	-10	mm
E_x	$(0.75 * R_r - \delta) * cos(\theta_2)$	
E_y	$(0.75 * R_r - \delta) * sin(\theta_2)$	
R_{AE}	$\sqrt{(((R_r * cos(\theta_1 + \theta_2)) - ((0.75 * R_r - \delta) * cos(\theta_2)))^2 + ((R_r * sin(\theta_1 + \theta_2)) - ((0.75 * R_r - \delta) * sin(\theta_2)))^2)}$	mm
R_r	55	mm
R_{shaft}	15	mm
x_{FE}	$E_x + ((E_x * R_{AE})/\sqrt{(E_x^2 + E_y^2)})$	mm
y_{FE}	$E_y + ((E_y * R_{AE})/\sqrt{(E_x^2 + E_y^2)})$	mm
R_{OK}	$\sqrt{(x_{FE}^2 + y_{FE}^2)}$	mm
B_x	$(R_r - h_f) * cos(\theta_1 + \theta_2)$	
B_y	$(R_r - h_f) * sin(\theta_1 + \theta_2)$	
C_x	$(R_r - h_f) * cos(\theta_2)$	
C_y	$(R_r - h_f) * sin(\theta_2)$	
R_{FD}	$\sqrt{((D_x - F_x)^2 + (D_y - F_y)^2)}$	mm
R_{OJ}	$F_x + R_{FD}$	
R_m	$IF(R_{OK} > R_{OJ}, R_{OK}, R_{OJ})$	mm
h_a	0.7	mm

TABLE 3. Design data set for inner arc of rare earth PM.

Name	Value	Evaluated Value
Start Point	D_x ,D_y ,0mm	53.13mm , 14.24mm , 0mm
Center Point	0 ,0 ,0	0mm , 0mm , 0mm
Angle	$-2 * \theta_2$	-30deg

TABLE 4. Design data set for outer arc of rare earth PM.

Name	Value	Evaluated Value
Start Point	D_x ,D_y ,0mm	53.13mm , 14.24mm , 0mm
Center Point	F_x ,F_y ,0mm	46.67mm , 0mm , 0mm
Angle	$-2 * \theta_{arc}$	-131.2deg

multiple design parameters. Selected design parameters and their respective ranges are presented in (15). These ranges are selected to satisfy the structural contrarians of the machine (to ensure design data does not violate the geometry of the six pole rotor structure). Design parameters are visually illustrated in Fig 3. As listed in 15), 7 distinct design parameters are considered. Any minor changes in these parameters could have a significant impact on the flux waveform. The reason for selecting 10,000 data points is to ensure the impacts of each parameter on the flux waveform are fully and accurately captured. In other words, to accurately train the model, a relatively small step size and therefore, relatively high number of simulation runs (i.e., 10,000) are required.

TABLE 5. Dataset formatting for deep learning.

Input								Output
$\mathbf{R_r}$	$\mathbf{h_a}$	α	δ	$\mathbf{h_f}$	θ_1	θ_2	θ	$\mathbf{B_{rad}}$
R_{r1}	h_{a1}	α_1	δ	h_{f1}	θ_{11}	θ_{21}	0^o	B_{rad11}
R_{r1}	h_{a1}	α_1	δ	h_{f1}	θ_{11}	θ_{21}	0.36^o	B_{rad12}
R_{r1}	h_{a1}	α_1	δ	h_{f1}	θ_{11}	θ_{21}	0.72^o	B_{rad13}
⋮	⋮	⋮	⋮	⋮	⋮	⋮	⋮	⋮
R_{r1}	h_{a1}	α_1	δ	h_{f1}	θ_{11}	θ_{21}	360^o	B_{rad1n}

$$\Omega = \begin{cases} 55 \le R_r \le 57 \\ 0.5 \le h_a \le 0.7 \\ 10 \le \alpha \le 0 \\ 10 \le \delta \le 3 \\ 3 \le h_f \le 7 \\ 10 \le \theta_1 \le 15 \\ 10 \le \theta_2 \le 15 \end{cases} \tag{15}$$

10,000 parameter sets are generated from the ranges specified in (15), and are clustered into n=10 groups to run n=10 parametric analysis, each with 1000 parameter sets. The FE software is programmed to run four parallel parametric simulations at a time in order to make data acquisition faster. The radial air-gap magnetic flux density for one parametric set (i.e., 1000 simulations) is captured and plotted along 360 mechanical degrees in Fig. 7. For every single FE simulation the total of 1000 data points at the midpoint of the air-gap along the machine circumference are collected (equivalent to the total of 10,000,000 data points for 10,000 parametric analysis). In other words, each of the flux waveform in Fig. 7 is constructed by connecting 1000 flux data points around the circumferential angle in the air-gap. The simulation is performed with a computer with 12 core (3.8Ghz) AMD Ryzen 9 3900X CPU and 32 GB (3200MHz) RAM and one set of parametric analysis (i.e., 1000 simulation) approximately took one hour. The sample data format for one parameter set is presented in Table 5. where B_{rad1n} refers to the air-gap radial flux density at n^{th} point along the air-gap circumference.

Once the FE parametric analysis for 10,000 text cases is complete, the corresponding flux data are used in Python [14] to train deep neural network (DNN) model using TensorFlow [15] and Keras [16] after normalization.

Normalization is performed on a data set to transform the data onto a similar scale. Normalization method adopted here is Min-max normalization, which is a linear transformation technique that gets all the scaled data in the range of (0, 1).

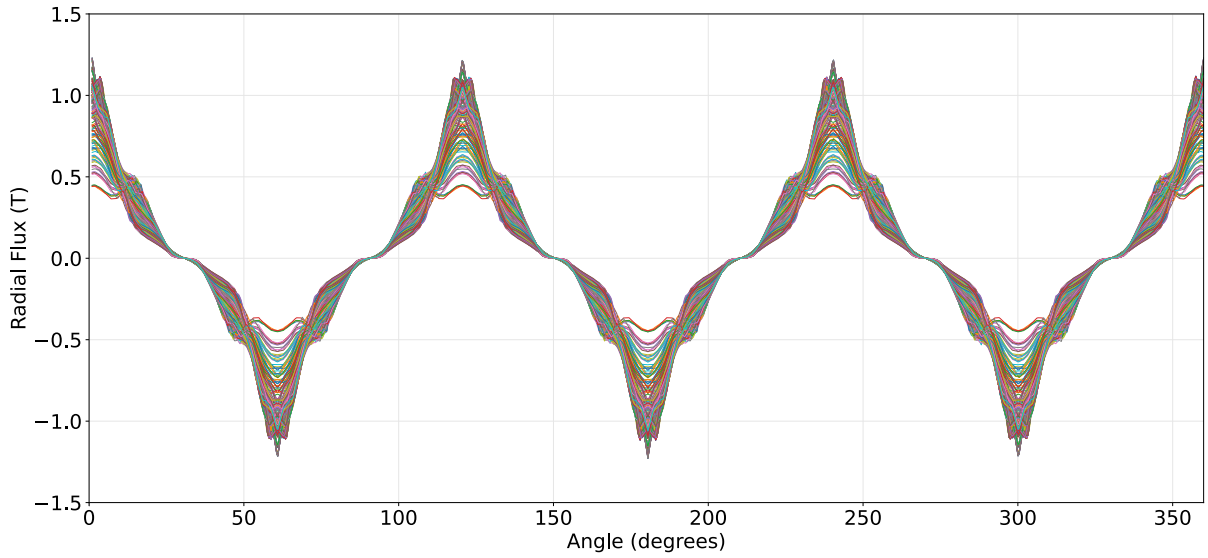

FIGURE 7. FE simulation result of parametric analysis.

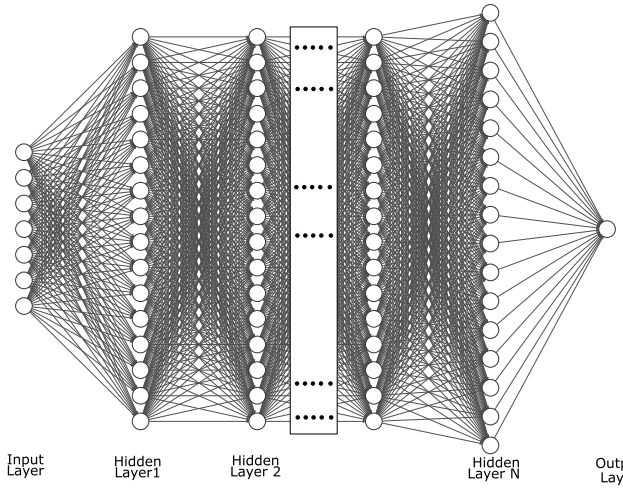

FIGURE 8. Deep neural network designed in python.

The implementation is as follows:

$$x_{scaled} = \frac{x - x_{min}}{x_{max} - x_{min}} \tag{16}$$

The DNN model is presented in Fig. 8. The model consists of 1 input layer, 10 hidden layers and 1 output layer. The input layer and hidden layer $H1$ are densely connected and activated by rectified linear activation (ReLU) function. All the hidden layers are densly connected with each other and also activated by ReLU function. The last hidden layer is connected to the output layer and activated by linear activation. To train the model a total of 500 epochs (iterations) are ran with data shuffle feature enabled. A ratio of 0.3 is chosen for validation split (i.e., data points are split into two smaller dataset containing 70% and 30% of the data). 70% of the data is used for training the model and the remaining 30% is used for testing. The reason that testing data sets are separated from the training sets is to avoid test results being biased toward the trained model. The loss (prediction error between the predicted value and actual value) in the model is calculated using mean square error (MSE) [16]. The optimization of the DNN model is conducted via adam optimizer [17]. For the given computer workstation computing power, the number of data points, and the total number of training iterations the training time is approximately 4 hours.

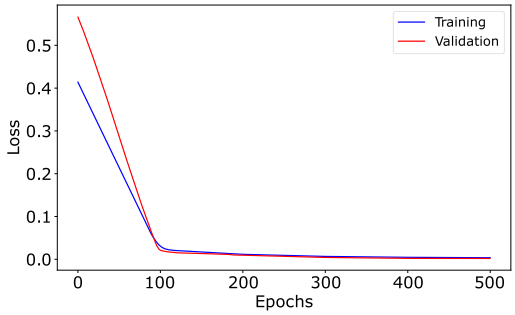

FIGURE 9. Training vs. validation loss for 500 epochs.

IV. DNN PREDICTION RESULTS, DISCUSSION AND OPTIMIZATION

To verify the accuracy of the established DNN model the training and validation losses for each of the 500 training iterations are calculated and plotted in Fig. 9. From trend of training and validation (testing) loss (Fig. 9) it can be inferred that the trained model works well and the model is not under/over fitted as the validation loss decreases to a stable point and has very minimal difference as compared to the testing loss in later epochs.

A. PRIMITIVE MAGNETIC FLUX DENSITY PREDICTION

The profile of the DNN predicted magnetic flux density in the air-gap is compared against the FE simulated results at five different test cases and the respective results are presented in

TABLE 6. Test cases for DNN prediction.

Case #	$\mathbf{R_r}$	$\mathbf{h_a}$	α	δ	$\mathbf{h_f}$	θ_1	θ_2
1	55.2	0.73	10.5	9	3.3	10.4	10
2	55	0.7	10	8	3	10	10
3	56.5	0.73	6	10	2.8	10	12
4	57	0.7	6	2	2.6	10.3	14
5	57	0.7	6.2	8	4.5	12	12

Fig. 10. As observed the DNN predicted and FE simulated air-gap flux density waveforms are in close agreement. The value of design parameters for each of the five test cases is presented in Table 6.Since each of case has a unique magnet size and rotor radius, the corresponding flux profile is quiet different from one case to another.

B. MODULATED MAGNETIC FLUX DENSITY CALCULATION

The primitive magnetic flux density in the air-gap obtained in Section IV-A is modulated by the stator slot/ tooth. The stator section includes 36 slots, and tooth pitch ratio ($a_s = (\theta_y - \theta_x)/\theta_s$) of 0.4 as shown in Fig. 11 and Fig. 12, respectively. To account for modulating effects of stator slots, the magnetic permeance function is derived using conformal mapping and multiplied by the primitive magnetic flux waveform.

To facilitate the derivation of the permeance function, stator tooth representation in S plane (Fig. 12) is transformed to K plane (Fig. 13) via conformal mapping [18]. The presented conformal transformation includes four sets of differential equations at four different stages; (i) S plane to Z plane (17), (ii) Z plane to W plane (18), (iii) W plane to T plane (19) and (iv) T plane to K plane (20).

$$\frac{\delta z}{\delta s} = \frac{1}{s} \tag{17}$$

$$\frac{\delta w}{\delta z} = -j\frac{\pi}{g'}\frac{(w-1)w}{(w-a)^{\frac{1}{2}}(w-b)^{\frac{1}{2}}} \tag{18}$$

$$\frac{\delta t}{\delta w} = j\frac{g'}{\pi}\frac{1}{w} \tag{19}$$

$$\frac{\delta k}{\delta t} = e^t = e^{ln(k)} = k \tag{20}$$

where,

$$b = \left[\frac{b'_o}{2g'} + \sqrt{\left(\frac{b'_o}{2g'}\right)^2 + 1}\right]^2, \; a = \frac{1}{b} \tag{21}$$

$$g' = ln\left(\frac{R_s}{R_r}\right) \tag{22}$$

$$b'_o = \theta_y - \theta_x \tag{23}$$

and R_s is inner radius of stator tooth.

Case # 1 from Table 6 is selected as a test case to derive the permeance function,and to serve as the benchmark for the optimization process. Inserting the geometric data of test

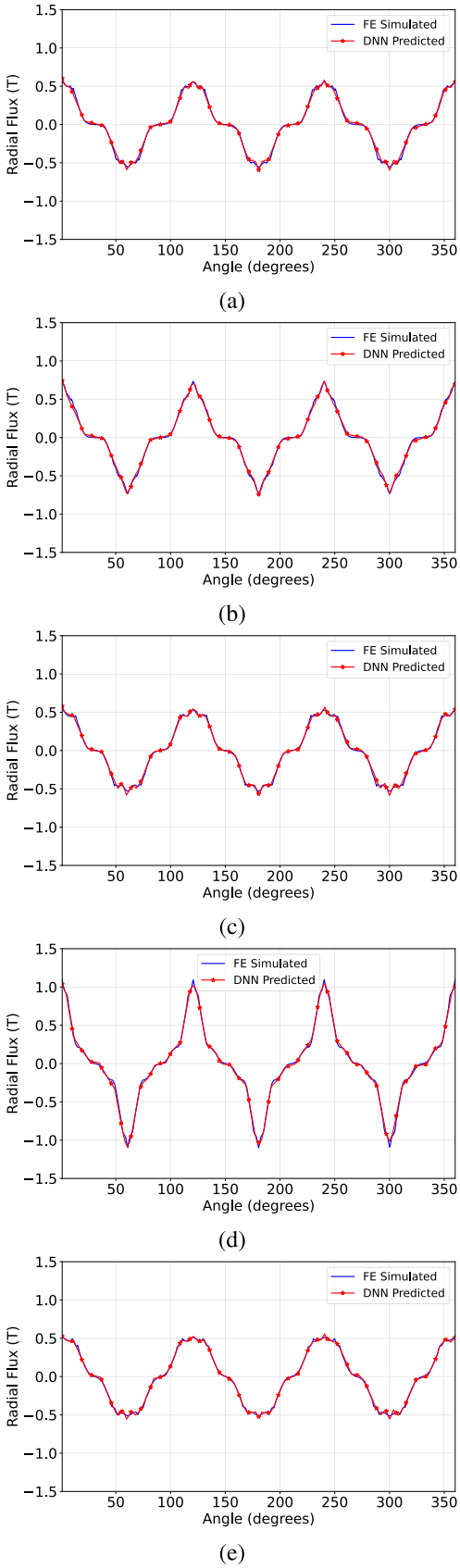

FIGURE 10. FE simulated vs. DNN predicted airgp radial flux density (a) case 1, (b) case 2, (c) case 3, (d) case 4 and (e) case 5.

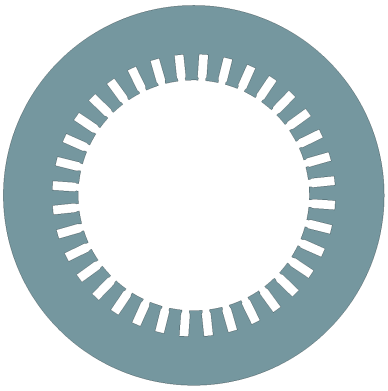

FIGURE 11. Structure of slotted stator.

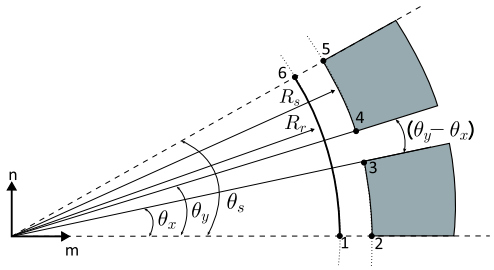

FIGURE 12. Infinitely deep slot in the *S* plane.

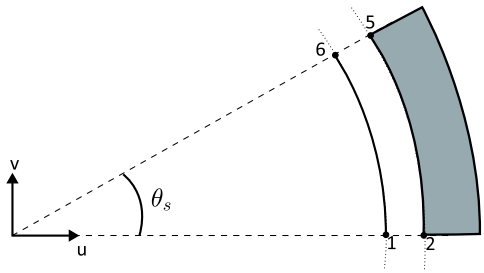

FIGURE 13. Stator slot representation in *K* plane.

Case # 1 in to (10) and (14) and using (24), the maximum distance of the magnetic structure from center is calculated as $R_m = 61.2mm$.

$$R_m = \begin{cases} R_{OK} & \text{if } R_{OK} > R_{OJ} \\ R_{OJ} & \text{otherwise} \end{cases} \tag{24}$$

The real part of the permeance function is calculated based on (17-20) and plotted along the angular length of a slot pitch in Fig. 14. The DNN predicted primitive magnetic flux density (F_M) is multiplied with the permeance function (Λ) to obtained the modulated air-gap flux density (25) (Fig. 15). For verification purposes, the profile of the modulated flux is compared against FE.

$$B(\theta) = F_M(\theta) \times \Lambda(\theta) \tag{25}$$

C. OPTIMIZATION

Next, the modulated flux density is optimized using Genetic Algorithm (GA), a population-based search method inspired

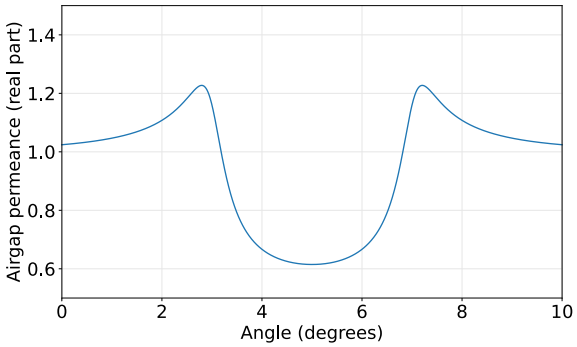

FIGURE 14. Real part of the derived permeance function along one slot pitch.

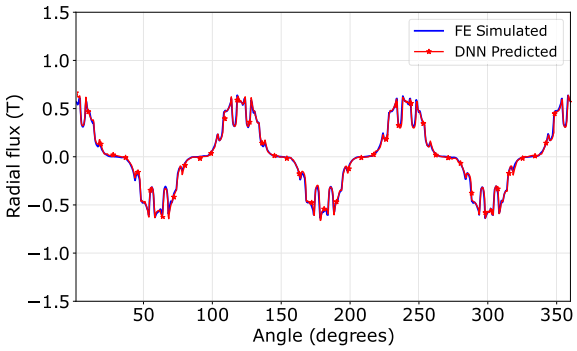

FIGURE 15. The profile of the modulated air-gap flux density.

TABLE 7. Optimized parameter set.

	$\mathbf{R_r}$	$\mathbf{h_a}$	α	δ	$\mathbf{h_f}$	θ_1	θ_2	THD %
Initial	55.2	0.73	10.5	9	3.3	10.4	10	36.57
Optim.	55.2	0.7	7.5	7.2	5.1	14.9	13.8	23.7

by the theory of natural evolution [19]. Fig. 16 presents the flow chart representation of GA. The objectives of the optimization are set as (i) minimize the flux harmonic content, and (ii) minimize cogging torque, by changing the geometrical parameters of the machine. The total harmonic distortion (THD) is selected as the objective function with the same constraints listed in (15).

The geometrical data for the optimized structure and the initial structure are presented in Table 7.

The modulated airgap flux density waveform and the cogging torque profile of the optimized structure are plotted and compared with the initial structure in Fig. 17 and Fig. 18, respectively. Analysing flux and torque waveform reveals 12.91% reduction of the THD level (from 36.57% to 23.66%) and 58.7% reduction in cogging torque.

The profile of the cogging torque is highly sensitive to the length, size and position of the magnets as extensively documented in the literature. Examples include [5], [20], [21], and [22]. Since the cogging torque is generated due to the interaction of the rotor MMF harmonics with the air-gap permeance function any minor change in these parameters

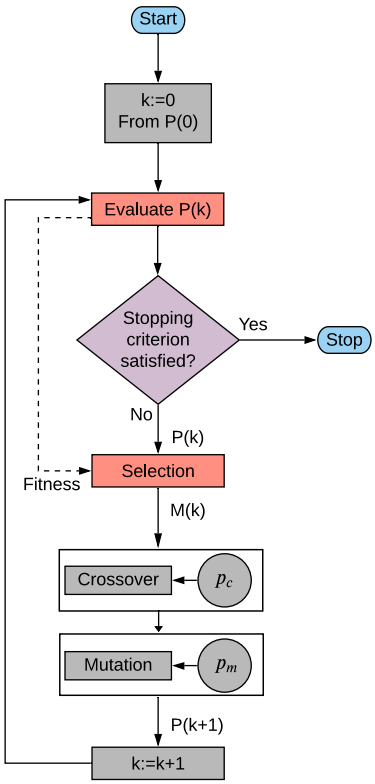

FIGURE 16. GA implementation flowchart.

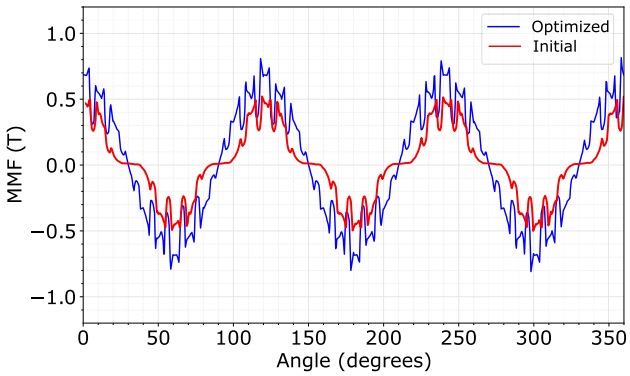

FIGURE 17. Profile of airgap flux density.

(i.e. change in magnet size or shape, rotor size or shape, and stator slot/tooth size or shape) may have a significant impact on the flux harmonics, and ultimately the cogging torque profile. By the same token, if magnets are slightly shifted or skewed would result in a notable change in the cogging torque profile in terms of amplitude and/or shift/delay along the x-axis.

It is noted that in both initial and optimized cases the cogging torque periodicity angle (τ_{cog}) is the same. In theory, the cogging torque periodicity angle (τ_{cog}) is a function of the least common multiple (LCM) between the stator slot

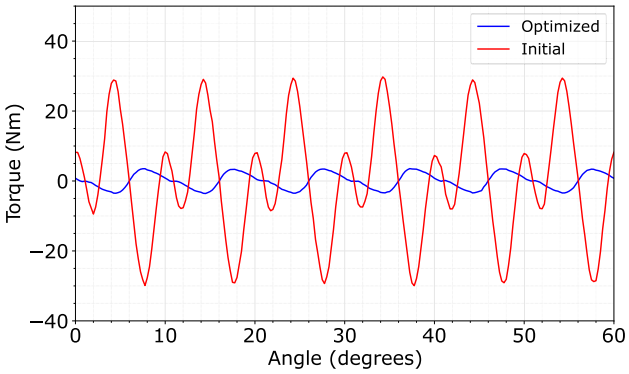

FIGURE 18. Cogging torque profile.

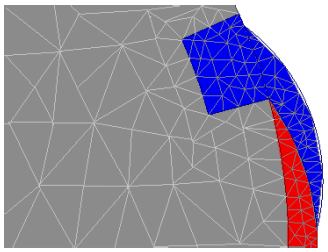

FIGURE 19. Meshing in FE software.

number (Q_s) and the rotor pole number ($2p$) as expressed in relation (26) [10]. The presented case study in this paper includes 6 poles and 36 slots, and therefore the cogging torque periodicity is theoretically expected to be 10^o degrees. This is consistent with the waveform shown Fig. 18.

$$\tau_{cog} = \frac{360^o}{LCM(Q_s, 2p)} \tag{26}$$

V. CONCLUSION

A deep learning-based design methodology was presented and applied to a complex case study with a hybrid magnetic structure. The total number of 7,000 geometrical data sets and their corresponding FE simulated results were used for training the model, and 3,000 samples for cross-validation. The 10,000 sample number is arbitrary and was chosen based on multiple criteria such as precision and speed. For further verification, the accuracy of the DNN-predicted flux waveform was confirmed via FE for a random given set of design parameters. The predicted DNN model was utilized to optimize the machine's structure with specific focus on flux harmonics and the cogging torque. Since optimization data were all provided via the trained model (the optimization stage was disassociated with FE), the presented solution lowers the computational burden compared to FE-based optimization solutions. Although the training data are generated via FE-simulation, it only involves magnetostatic solver. In fact, transient analyses are all preformed efficiently using the trained model as opposed to using the FE model. The proposed approach is general and can be applied to all types of electric machines.

APPENDIX

The FE-based modeling features and detailed simulation setup are as follows:

- Solution setup: Adaptive
  - Maximum number of passes: 10
  - Percentage error: 1 %
- Meshing: "Inside Selection" meshing was selected which applies meshes through the entire volume of the object. Further details of meshing are:
  - Maximum mesh length for magnets: 1 mm
  - Maximum mesh length for stator and rotor: 5 mm

  The meshing for the proposed design is presented in Fig. 19. After each simulation pass, the mesh is refined by the FE simulation software (create denser meshes) in order to reduce the solution error.

REFERENCES

[1] B. Poudel, E. Amiri, P. Rastgoufard, and B. Mirafzal, "Toward less rare-Earth permanent magnet in electric machines: A review," *IEEE Trans. Magn.*, vol. 57, no. 9, pp. 1–19, Sep. 2021.
[2] H. Hua, "Partitioned stator machines with NdFeB and ferrite magnets," *IEEE Trans. Ind. Appl.*, vol. 53, no. 3, pp. 1870–1882, May/Jun. 2017.
[3] X. Zhu, W. Wu, L. Quan, Z. Xiang, and W. Gu, "Design and multi-objective stratified optimization of a less-rare-earth hybrid permanent magnets motor with high torque density and low cost," *IEEE Trans. Energy Convers.*, vol. 34, no. 3, pp. 1178–1189, Sep. 2019.
[4] Q. Chen, G. Liu, W. Zhao, M. Shao, and Z. Liu, "Design and analysis of the new high-reliability motors with hybrid permanent magnet material," *IEEE Trans. Magn.*, vol. 50, no. 12, pp. 1–10, Dec. 2014.
[5] B. Poudel, E. Amiri, and P. Rastgoufard, "Analytical investigation and heuristic optimization of surface mounted permanent magnet machines with hybrid magnetic structure," *IEEE Open J. Ind. Appl.*, vol. 3, pp. 152–163, 2022.
[6] M. M. Ghahfarokhi, V. Z. Faradonbeh, E. Amiri, S. M. M. Bafrouei, A. D. Aliabad, and S. T. Boroujeni, "Computationally efficient analytical model of interior permanent magnet machines considering stator slotting effects," *IEEE Trans. Ind. Appl.*, vol. 58, no. 4, pp. 4587–4601, Jul. 2022.
[7] H. Sasaki, Y. Hidaka, and H. Igarashi, "Explainable deep neural network for design of electric motors," *IEEE Trans. Magn.*, vol. 57, no. 6, pp. 1–4, Jun. 2021.
[8] A. Khan, M. H. Mohammadi, V. Ghorbanian, and D. Lowther, "Efficiency map prediction of motor drives using deep learning," *IEEE Trans. Magn.*, vol. 56, no. 3, pp. 1–4, Mar. 2020.
[9] E. Ghosh, A. Mollaeian, S. Kim, J. Tjong, and N. C. Kar, "DNN-based predictive magnetic flux reference for harmonic compensation control in magnetically unbalanced induction motor," *IEEE Trans. Magn.*, vol. 53, no. 11, pp. 1–7, Nov. 2017.
[10] V. Z. Faradonbeh and E. Amiri, "Open-circuit electromagnetic analysis of interior permanent magnet machines with arbitrary rotor frame using a 2-D analytical model," *IEEE Trans. Magn.*, vol. 58, no. 8, pp. 1–12, Aug. 2022.
[11] V. Z. Faradonbeh, A. Rahideh, M. M. Ghahfarokhi, E. Amiri, A. D. Aliabad, and G. A. Markadeh, "Analytical modeling of slotted, surface-mounted permanent magnet synchronous motors with different rotor frames and magnet shapes," *IEEE Trans. Magn.*, vol. 57, no. 1, pp. 1–13, Jan. 2021.
[12] X. Wang, Y. Yang, and D. Fu, "Study of cogging torque in surface-mounted permanent magnet motors with energy method," *J. Magn. Magn. Mater.*, vol. 267, no. 1, pp. 80–85, Nov. 2003. [Online]. Available: https://www.sciencedirect.com/science/article/pii/S030488530300324X
[13] J. Kolehmainen, "Dovetail permanent magnet rotor solutions with different pole numbers," in *Proc. 18th Int. Conf. Electr. Mach.*, Sep. 2008, pp. 1–4.
[14] G. Van Rossum and F. L. Drake, *Python 3 Reference Manual*. Scotts Valley, CA, USA: CreateSpace, 2009.
[15] M. Abadi. (2015). *TensorFlow: Large-Scale Machine Learning on Heterogeneous Systems*. Software. [Online]. Available: https://www.tensorflow.org/
[16] F. Chollet. (2015). *Keras*. [Online]. Available: https://keras.io
[17] D. P. Kingma and J. Ba, "Adam: A method for stochastic optimization," 2014, *arXiv:1412.6980*.
[18] D. Žarko, D. Ban, and T. A. Lipo, "Analytical calculation of magnetic field distribution in the slotted air gap of a surface permanent-magnet motor using complex relative air-gap permeance," *IEEE Trans. Magn.*, vol. 42, no. 7, pp. 1828–1837, Jul. 2006.
[19] E. K. Chong and S. H. Zak, *An Introduction to Optimization*. Hoboken, NJ, USA: Wiley, 2004.
[20] N. Bianchi and S. Bolognani, "Design techniques for reducing the cogging torque in surface-mounted PM motors," *IEEE Trans. Ind. Appl.*, vol. 38, no. 5, pp. 1259–1265, Sep./Oct. 2002.
[21] G. Bramerdorfer, E. Marth, and G. Goldbeck, "Cogging torque sensitivity considering imperfect magnet positioning for permanent magnet machines of different slot and pole count," *CES Trans. Electr. Mach. Syst.*, vol. 4, no. 3, pp. 243–251, Sep. 2020.
[22] J. Rao, Y. Gao, D. Li, and R. Qu, "Performance analysis of interior permanent magnet motor using overlapping windings with fractional ratio of slot to pole pair," *IEEE Trans. Appl. Supercond.*, vol. 26, no. 7, pp. 1–5, Oct. 2016.

BIKRANT POUDEL (Graduate Student Member, IEEE) received the B.S. degree in electronics and communication engineering from Tribhuvan University, Kathmandu, Nepal, in 2013, and the M.S. degree in electrical engineering and the Ph.D. degree in engineering and applied science from The University of New Orleans, New Orleans, LA, USA, in 2017 and 2022, respectively. He is currently working as an Associate Professor with Exponent Inc., and an Adjunct Faculty Member with The University of New Orleans. His current research interests include motor design and optimization and grid-connected PV.

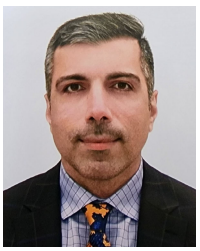

EBRAHIM AMIRI (Senior Member, IEEE) received the B.Sc. and M.Sc. degrees in electrical engineering from the Amirkabir University of Technology, Tehran, Iran, in 2005 and 2008, respectively, and the Ph.D. degree in electrical engineering from Louisiana State University, Baton Rouge, LA, USA, in 2013. He is currently an Associate Professor and the Chair of the Department of Electrical and Computer Engineering, The University of New Orleans, New Orleans, LA, USA. His current research interests include the design, modeling, and optimization of electromagnetic devices.